X-ray Diffraction, NMR Studies, and DFT Calculations of the Room and High Temperature Structures of Rubidium Cryolite, Rb 3 AlF 6

Aydar Rakhmatullin, František Šimko, Emmanuel Véron, Mathieu Allix, Charlotte Martineau-Corcos, Andy Fitch, Franck Fayon, Roman A Shakhovoy, Kirill Okhotnikov, Vincent Sarou-Kanian, et al.

X-ray diffraction, NMR studies, and DFT calculations of the room and high temperature structures of rubidium cryolite, Rb_3AlF_6

Aydar Rakhmatullin*,†, František Šimko*,‡,†, Emmanuel Véron†, Mathieu Allix†, Charlotte Martineau-Corcos†,§, Andy Fitch‖, Franck Fayon†, Roman A. Shakhovoy†, Kirill Okhotnikov†, Vincent Sarou-Kanian†, Michal Korenko‡, †, Zuzana Netriová‡, Ilja B.Polovov⁋, and Catherine Bessada†

† Conditions Extrêmes et Matériaux: Haute Température et Irradiation, CEMHTI, UPR 3079 -CNRS Univ. Orléans 45071, Orléans, France.

‡ Institute of Inorganic Chemistry, Slovak Academy of Sciences, 845 36 Bratislava, Slovakia.

† Centre of Excellence for advanced Materials Application - CEMEA, Slovak Academy of Sciences, Dúbravská cesta 5807/9, 845 11 Bratislava, Slovakia

§ Université de Versailles Saint-Quentin en Yvelines, 45 Avenue des Etats-Unis, 78035 Versailles Cedex, France

‖ ID22, ESRF, Grenoble, France

⁋ Department of Rare Metals and Nanomaterials, Institute of Physics and Technology Ural Federal University, Ekaterinburg, Russia

KEYWORDS rubidium cryolite, Rb_3AlF_6, phase transitions, solid-state NMR, X-ray powder diffraction, CASTEP

ABSTRACT: A crystallographic approach incorporating multinuclear high field solid state NMR (SSNMR), X-ray structure determinations, TEM observation, and density functional theory (DFT) was used to characterize two polymorphs of rubidium cryolite, Rb_3AlF_6. The room temperature phase was found to be ordered and crystallizes in the *Fddd* (n°70) space group with a = 37.26491(1) Å, b = 12.45405(4) Å, c = 17.68341(6) Å. Comparison of NMR measurements and computational results revealed the dynamic rotations of the AlF_6 octahedra. Using *in-situ* variable temperature MAS NMR measurements, the chemical exchange between rubidium sites was observed. The β-phase, i.e. high temperature polymorph, adopts the ideal cubic double-perovskite structure, space group $Fm\bar{3}m$, with a = 8.9930(2) Å at 600 °C. Additionally, a series of polymorphs of K_3AlF_6 has been further characterized by high field high temperature SSNMR and DFT computation.

INTRODUCTION

The binary system $RbF–AlF_3$ belongs to a bigger family of cryolitic systems $MF–AlF_3$ (M = Li, Na, K, Rb, Cs, Fr). While one member of this family, molten sodium cryolite ($NaF–AlF_3$), is the main constituent of the electrolyte for the industrial production of aluminum worldwide, the other members of that cryolitic family (Li, K, Rb) could have also been considered because of their role as the constituents for the new "low-melting" electrolytes in electrometallurgy.[1]

The structure of rubidium cryolite and the solubility of the alumina, with consequent formation of the electroactive species, is the principal task for the potential utilization of rubidium cryolite in the aluminium electrowinning. Little information is however available about Rb_3AlF_6 in open literature compared to, for example its analogues lithium, sodium and potassium cryolite (Li_3AlF_6,[2,3] Na_3AlF_6,[4-6] and K_3AlF_6,[7,8]). Holm analyzed the three cryolites K_3AlF_6, Rb_3AlF_6, and Cs_3AlF_6 by DTA and XRD methods.[9] Cooling curves of pure Rb_3AlF_6 contained two exothermic peaks: liquid-solid phase transition at 920 °C and the other modification transition at 357 °C. XRD investigations showed that the room temperature form of Rb_3AlF_6 has tetragonal symmetry, while its high temperature modification is assumed to be face-centered cubic. Chen and Zhang[10] studied the quenched samples of the system $RbF–AlF_3$ by DTA, DSC and XRD methods. Three compounds were identified: Rb_3AlF_6, $RbAlF_4$ and $RbAl_3F_7$. Rb_3AlF_6 melts congruently at 878 °C and its $\alpha \leftrightarrow \beta$ forms transformed reversibly at 340 °C. The crystal structures of both Rb_3AlF_6 modifications have not yet been completely described.

The cryolite systems of alkali metals could also have other industrial applications. Recently, Mn^{4+} activated K_3AlF_6 was studied as a potential red phosphor for warm white light-emitting diodes.[11] It shows an efficient luminous efficacy beyond 190 lm/W, along with an excellent color rendering index (Ra = 84) and a lower correlated color temperature (CCT = 3665 K). These types of materials with improved performance that can be industrially produced at competitive cost are needed in different fields of industry and particle physics research.[12,13]

The specific crystal structural features, phase transitions, and related physical properties of the cryolite materials can be linked to structural similarity with a larger group of materials known as elpasolite halides (after the name of the mineral elpasolite, K_2NaAlF_6). These materials have a "mixed-cation" fluoride perovskite-type structure, in which the corner-sharing octahedral network is made up of alternating (AlF_6) and ($Na(K)F_6$) octahedra. Elpasolite ($A_2BB'X_6$) and cryolite ($A_3B'X_6$) structure types derive from the perovskite by cationic ordering. Unlike simple ABX_3 perovskites, where all octahedra are equivalent, in elpasolites (also known as ordered perovskites), there are two kinds of non-equivalent ionic groups BX_6 and $B'X_6$ alternating along the three four-fold cubic axes. Numerous elpasolite-like crystals are known to undergo structural phase transitions or to exist in distorted phases up to the melting temperature.

The structures of K_3AlF_6,[7,8] Sr_3WO_6,[14] $Rb_2K(Cr\ or\ Ga)F_6$,[15] and $(K\ or\ Rb)_3MoO_3F_3$[16] are a small part of the elpasolite or double perovskite type which show non-cooperative octahedral tilting (NCOT). In these phases, one of the octahedra is rotated by ~45° while the other remains untilted. Some of the elpasolite-type materials are suitable for scintilators, showing desirable isotropic optical and mechanical properties.[17]

In this paper, we will present a new example of the structure of Rb_3AlF_6 with non-cooperative octahedral tilting and the first complex NMR investigation of such compounds like K_3AlF_6 and Rb_3AlF_6. We will present a characterization of the structure of rubidium cryolites using X-ray diffraction (XRD) and transmission electron microscopy (TEM). Both potassium and rubidium cryolites were characterized using various 1D and 2D solid state NMR techniques including *in-situ* HT MAS NMR. The interpretation of all experimental NMR results is significantly enhanced by the contribution of the first principle DFT calculations. We think that this computing approach was applied, for the first time, to such a complex structure.

EXPERIMENTAL SECTION

Preparation of pure compounds

K_3AlF_6

Potassium cryolite was prepared in a glovebox following the preparation detailed by Abakumov *et* al.[7] and Šimko *et* al.[18]

Rb_3AlF_6 and $RbAlF_4$

The synthesis protocol of rubidium cryolite was identical to that described in our previous work.[19] Rubidium tetrafluoroaluminate was prepared by heating a stoichiometric mixture of RbF and AlF_3. Two grams of mixture were mechanically homogenized in a glovebox under inert atmosphere (Ar - Messer, 99.999 % purity), placed in a Pt crucible and heated in a tightly closed vertical resistance furnace with water-cooling from room temperature to 600 °C, at a rate of 5 °C/min. The mixture was held for 1 hour at 20 bars to avoid the dissociation reaction, and then cooled to room temperature. XRD patterns is shown in Supporting Information (Figure S1).

Thermal analysis measurements

The classical thermal analysis was performed as described by Šimko et al.[19] in a Pt crucible with a lid. The cooling rate was 1.4 °C/min. By using such a slower cooling rate in a larger quantity of sample (10 grams), it was possible to detect the real temperature of primary crystallization of Rb_3AlF_6. The slow cooling rate is essential for the thermal analysis of materials like Rb_3AlF_6 which often show extended thermal dissociation.[20]

SSNMR measurements

Room temperature solid-state NMR experiments were carried out on a Bruker Avance III NMR spectrometers operating at 9.4 T and 20.0 T, using a 2.5 mm resonance probe at MAS frequency varying between 30 and 34 kHz. In addition, to enhance resolution in some of the ^{19}F solid state NMR experiments, we used a 1.3 mm probe to be able to rotate samples up to 67 kHz. ^{27}Al NMR spectra were acquired using a double frequency sweep (DFS) pulse due to a possibility of signal enhancement. The parameters of the dipolar ^{87}Rb-^{19}F HMQC[21,22] experiments were identical to our previous study.[19]

^{87}Rb MQMAS spectra were acquired with Z-filtering[23] and hypercomplex (States)[24] phase detection. A sweep width of 60 kHz and 120 kHz ($4\nu_r$) was used in the direct and indirect dimension, respectively. The optimized excitation and conversion pulse width was 4 μs (ν_{rf} = 62.5 kHz) and 1.3 μs (ν_{rf} = 192 kHz), respectively. A repetition delay was 0.66 s.

The *in-situ* high temperature NMR experiments were carried out on a Bruker Avance III HD NMR spectrometer operating at 17.6 T with resonance frequencies of 245.4 MHz and 705.8 MHz for ^{87}Rb and ^{19}F, respectively, employing a 7 mm Bruker laser MAS probe. The bottom-less MAS rotor is equipped with an inner container made from aluminium nitride (AlN) which carries the sample. Heating of the sample is achieved using a 200 W DILAS diode laser operating at 980 nm. The laser beam is fed through an optical fiber into the probe, the fiber ending ca. 1 cm underneath the stator, and then directed to the AlN container. The ^{27}Al background signal is very large hence no ^{27}Al NMR measurements were recorded. In all *in-situ* HT experiments, the MAS frequency was 5000 Hz. Because of the broad NMR patterns of ^{19}F and ^{87}Rb resulting from large chemical shift anisotropy and low MAS rate, two-dimensional (2D) NMR techniques, MATPASS[25] and QMATPASS,[26] for ^{19}F and ^{87}Rb respectively that able to separate the isotropic and the anisotropic chemical shifts in two different dimensions were

employed, as ideal approach to study our samples at very high temperature. They yield high-resolution NMR isotropic peaks free of CSA-related broadening in one dimension and the corresponding anisotropic powder sideband pattern for each isotropic peak, in the second dimension. The separation of the side bands has been carried out with 5-π MATPASS experiment for ^{19}F and 9-π QMATPASS pulse sequence for ^{87}Rb. Duration of the π pulse was 15.5 μs for ^{19}F and 10 μs for ^{87}Rb. To avoid the time conflict caused by the finite length of the pulse, even π pulses were placed at 2/3 and 4/3 of the rotor period in case of MATPASS and 2/5, 4/5, 6/5, and 8/5 of the rotor period in case of QMAT, such that the whole pulse sequences spanned almost $3\tau_r$ at first t_1 increment and $2\tau_r$ at the last one. 12-step and 20-step cogwheel phase cycling[27] was used to select the alternating coherence transfer pathway in MATPASS and QMATPASS experiments, respectively. Each t_1 increment was acquired at 48 transients for ^{19}F and at 1000 scans for ^{87}Rb.

^{19}F, ^{27}Al, and ^{87}Rb chemical shifts are referenced to $CFCl_3$, 1 M $Al(NO_3)_3$, and 0.01 M $RbNO_3$, respectively. The NMR parameters (chemical shifts, chemical shift anisotropies, asymmetry parameters, line widths, and quadrupolar parameters) were fitted for several different rotor frequencies and for two magnetic fields to the experimental spectra by means of the DMfit program.[28]

Temperature calibration

Temperature measurement in the case of laser heating cannot be performed directly; hence, an indirect calibration of the temperature was used. It is obvious that heating the container from only one side leads to a considerable temperature gradient in the sample. To reduce the value of the temperature gradient, a small amount of the powder was used (about 20 mg). The temperature calibration was performed using several reference compounds K_3AlF_6 (^{19}F spectra),[8, this paper] Rb_3AlF_6 (^{19}F and ^{87}Rb),[9, this paper] Na_2SiF_6 (^{23}Na),[29] and CuI, CuBr (^{63}Cu),[30] whose phase transition temperature is well defined. The laser power exhibits a temperature dependence given by Shakhovoy *et al.*[31] $P = aT^4+bT-c$, where a, b, c are constants, P is a percentage of the maximum laser power controlled by the experimenter. In addition, the calibration was double checked by employing the temperature dependence of the ^{79}Br MAS NMR signal of KBr:[32] $T=-40\times\delta_{iso}+RT$. In the temperature range 200-500 °C, the agreement between the two methods of calibration is highly satisfying (Figure S2).

First-Principles Calculations

Calculations of NMR parameters were identical to our previous study[18] and the computational details are presented in the Supporting Information. Linear regressions led to the following relationships for ^{19}F: $\delta_{iso}(ppm) = -0.795\times\sigma_{iso} + 89.444$.[33]

Electron diffraction

Electron diffraction patterns were collected on a Philips CM20 microscope fitted with an Oxford energy dispersive spectrometry (EDS) analyzer. In order to avoid rapid deterioration of the samples under the electron beam, a nitrogen-cooled sample holder was used.

Synchrotron Powder Diffraction

Synchrotron powder diffraction measurements were performed at the ESRF beamline ID22 (Grenoble, France) operating at the wavelength 0.32623 Å. The measurements were performed at several temperatures using a hot-air blower sensor while heating the Rb_3AlF_6 sample from room temperature up to 600 °C. A 12-min waiting time was used at each temperature step in order to ensure thermal equilibration, then powder synchrotron data was collected over the 0.5-48° 2θ with a 0.002° step size. Polycrystalline powder samples were sealed in 0.5 mm diameter borosilicate capillaries, which were rotated in order to reduce potential texture effects.

RESULTS

M_3AlF_6 (M= Li, Na, K) compositions generally belong to congruently melting compounds with one simple endothermic signature. During cooling, Li_3AlF_6 shows an endothermic peak corresponding to crystallization at 782-785 °C,[34] Na_3AlF_6 at 1011 °C,[1] and K_3AlF_6 at 974 °C.[9] The thermal endothermic effect of Rb_3AlF_6 was in this work obtained from the melt by thermal analysis at 920 °C (Figure S3). The whole thermal cooling curve also contains other endothermic delay located at 346 °C. This delay corresponds to the polymorphic solid transition of the high temperature β-modification of Rb_3AlF_6 to the low temperature of α-Rb_3AlF_6 (Figure S3, right). This is in good agreement with values previously reported by Holm,[9] Chen and Zhang.[10] The similar behavior of solid state crystal transformation is not unusual, even in between others M_3AlF_6 compounds. This behavior relates to the phase transition from high-temperature, high-symmetry modifications to a low-temperature, low symmetry forms. Li_3AlF_6, for example, forms four modifications: δ-, γ-, β-, and α-forms. High-temperature δ-form transforms to γ-form at 597 °C and $\gamma\leftrightarrow\beta$ transformation occurs at 510 °C.[2] Last $\beta\leftrightarrow\alpha$ equilibrium occurs at 210 °C.[3] On the other hand, Na_3AlF_6 forms only one solid-solid transformation. The cubic high-temperature β-Na_3AlF_6 is at 563 °C in equilibrium with the low-temperature monoclinic α-Na_3AlF_6.[5] Three phase transitions of K_3AlF_6 are identified at 306 °C, 153 °C, and 132 °C. The high-temperature δ-phase is at 306 °C in equilibrium with orthorhombic γ-phase. γ-phase forms at 153 °C an intermediate β-phase, which exists only in very narrow temperature intervals, and it is then being transformed at 132 °C to a stable monoclinic α-phase.[8]

α-Rb_3AlF_6

Although the crystal structure of Rb_3AlF_6 has not been described up to now, unit cell parameters and symmetry were previously proposed based on X-ray powder diffraction data.[10] Chen and Zhang suggested that the low temperature α form is orthorhombic with a = 7.748(5) Å, b = 5.365(3) Å, and c = 4.388(2) Å while the high temperature β one is cubic with a = 7.612(4) Å.

Diffraction data.

Using high-resolution synchrotron powder diffraction data, we first performed an auto-indexing analysis of the

room temperature phase. The orthorhombic cell dimensions a = 37.2649 Å, b = 12.4541 Å and c = 17.6834 Å were determined with good reliability factors by indexing using Dicvol[40] and Treor[41] programs and by analyzing the peak positions in the powder synchrotron patterns. These cell parameters strongly differ from the proposed indexation of α-Rb_3AlF_6.[10] A subsequent ICDD database search using similar cell parameters, volume tolerance fixed at 10 %, and chemistry restrictions (only alkali metals, transition metals, and fluorine) resulted in one compound with similar indexation: γ-K_3AlF_6 (ICSD 262077). This compound crystallizes in the *Fddd* space group. The proposed orthorhombic indexation was then tested via a LeBail fit of the SPD pattern, and the obtained good reliability factors (R_{wp} = 5.48 %, R_p = 3.31 %, and G.O.F. = 0.7) confirmed that α-Rb_3AlF_6 appears isostructural to γ-K_3AlF_6. Moreover, the cell parameters and the space group *Fddd* of the rubidium cryolite compound was confirmed by an electron diffraction study (Figure 1).

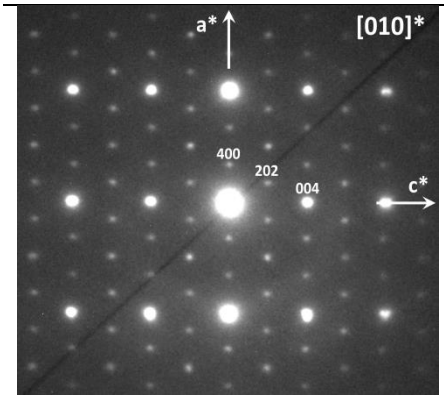

Figure 1. [010] selected area electron diffraction pattern of α-Rb_3AlF_6. Indexed in the a = 37.27 Å, b = 12.45 Å and c = 17.68 Å cell with a *Fddd* space group.

In order to precisely determine the structure of α-Rb_3AlF_6, a Rietveld refinement of the SPD pattern was performed. The starting model was based on the γ-K_3AlF_6 structure using the orthorhombic cell parameters previously determined by auto-indexing methods and replacing potassium by rubidium atom. Both cationic and fluorine positions, as well as atomic displacement parameters, were refined (Table 1). Good reliability factors were obtained (R_{wp}=6.23 %, R_p=4.12 % and GOF=0.8). The Rietveld refinement also allowed the identification of a secondary phase of $RbSiO_4$, which quantification was determined as 2.45(5) wt%. This phase is probably a result of a contamination caused by a reaction of RbF and the ceramic materials (alumino-silicate tube) in the furnace when the synthesis was performed.

The fit of the SPD Rietveld refinement is shown in Figure 2. Atomic coordinates, atomic displacement parameters and Rb–F and Al–F interatomic distances are summarized in Tables 2 and S1.

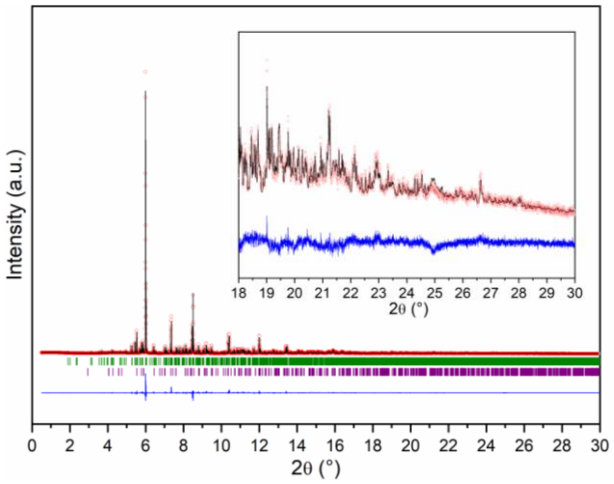

Figure 2. Experimental (red), calculated (black), and difference (blue) SPD Rietveld refinement of α-Rb_3AlF_6 (green marks); the Bragg peaks position of the secondary phase $RbSiO_4$ as impurity were visible in purple. An enlargement of the 18-30° range is embedded.

Table 1. Crystallographic data for the polymorphs of Rb_3AlF_6 from XRD Rietveld refinement.

Chemical formula	α-Rb_3AlF_6	β- Rb_3AlF_6
Source	synchrotron	synchrotron
Formula weight ($g.mol^{-1}$)	397.4	397.4
Temperature (°C)	RT (20)	600
Wavelength (Å)	0.32623	0.32623
Crystal system	Orthorhombic	Cubic
Space group	*Fddd* (n°70)	$Fm\bar{3}m$ (n°225)
Unit cell dimensions (Å)	a = 37.26491(1) b = 12.45405(4) c = 17.68341(6)	a = 8.9930(2)
Cell volume ($Å^3$)	8206.85	727.30
Z	48	4
d-space range	0.4-37	0.4-37
χ^2	0.8	0.89
R_p (%)	4.12	4.7
R_{wp} (%)	6.23	7.92

For definition of R-factors see reference 40-41.

Table 2. Atomic coordinates and Atomic Displacement Parameters of α-Rb_3AlF_6 determined from Rietveld Refinement of synchrotron powder diffraction data collected at room temperature.

Atom	Wyckoff site	Occupancy	x/a	y/b	z/c	U_{iso} / Å^2
Rb1	32h	1	0.19678(3)	0.40398(1)	0.12410(9)	0.0295(6)
Rb2	16g	1	0.125	0.125	0.41691(9)	0.0281(8)
Rb3	32h	1	0.12419(6)	0.34203(9)	0.2649147)	0.0283(6)
Rb4	32h	1	0.20933(4)	0.1216(2)	0.24863(9)	0.0279(6)
Rb5	32h	1	0.21713(4)	0.1287(2)	0.76400(8)	0.0319(6)
Al1	8a	1	0.25	0.125	0.125	0.019(4)
Al2	8b	1	0.125	0.625	0.125	0.013(3)
Al3	16e	1	0.28964(2)	0.125	0.125	0.024(3)
Al4	16e	1	0.45799(2)	0.125	0.125	0.008(2)
F1	32h	1	0.15945(2)	0.0253(5)	0.1247(7)	0.060(3)
F2	16g	1	0.125	0.125	0.2280(4)	0.018(3)
F3	32h	0.527(1)	0.1664(4)	0.6193(2)	0.1705(6)	0.037(3)
F4	32h	0.348(1)	0.1023(8)	0.557(2)	0.1958(1)	0.023(6)
F5	32h	0.632(1)	0.1194(4)	0.7414(9)	0.1866(8)	0.033(3)
F6	32h	1	0.28934(2)	0.1185(1)	0.0246(3)	0.030(2)
F7	32h	1	0.25429(2)	0.2272(5)	0.1210(8)	0.028(2)
F8	32h	1	0.32447(2)	0.0210(5)	0.1181(7)	0.028(2)
F9	32h	1	0.45774(2)	0.1357(1)	0.0232(3)	0.036(2)
F10	32h	1	0.49293(2)	0.2279(5)	0.1301(8)	0.034(2)
F11	32h	1	0.42444(2)	0.0231(5)	0.1318(7)	0.035(2)

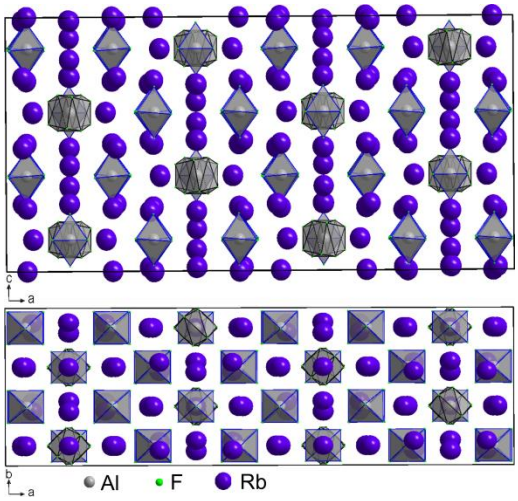

Figure 3. Projections of the unit cell structure of α-Rb_3AlF_6 in the (010) and (001) planes.

Solid-state NMR data.

Both room temperature ^{27}Al MAS NMR spectra (Figure S4) recorded at two magnetic fields of 9.4 and 20 T show a single narrow peak (full width at half-maximum, FWHM = 135 Hz) in the octahedral region at $\delta_{iso}(^{27}Al)$ = 0.0 ppm. All four aluminum sites give rise to overlapping resonances, indicating that their environments in the structure are similar and symmetrical. The ^{19}F MAS (34 kHz) NMR spectrum of α-Rb_3AlF_6 recorded at 20 T revealed four signals located at -142.0, -143.5, -145.1 and -148.0 ppm with relative intensities of 1:2:1:2, respectively (Figure 4a). We know from the powder diffraction that the crystal structure is described based on 11 inequivalent fluorine atoms: F2 occupies a site 16*g*, F1, F6-F10 fully occupy a position 32*h* while F3, F4 and F5 partially occupy their 32*h* position. It means that at least 12 ^{19}F resonances with relative intensity 1 for F2, 2 for F6-F10, 1 for F3, 0.7 for F4 and 1.3 for F5 can be expected in the ^{19}F MAS NMR spectrum.

The ^{87}Rb MAS NMR spectrum shows three different kinds of Rb atoms environments and the presence of overlapping quadrupolar resonances (Figure 5a). To improve the resolution, we have used the two dimensional ^{87}Rb MQMAS technique at two magnetic fields, 9.4 T and 20 T (Figure S5 and 5b), which reveals the presence of five resonances. The whole set of 1D and 2D ^{87}Rb NMR spectra recorded at different fields were modeled using a single consistent set of parameters given in Table 3.

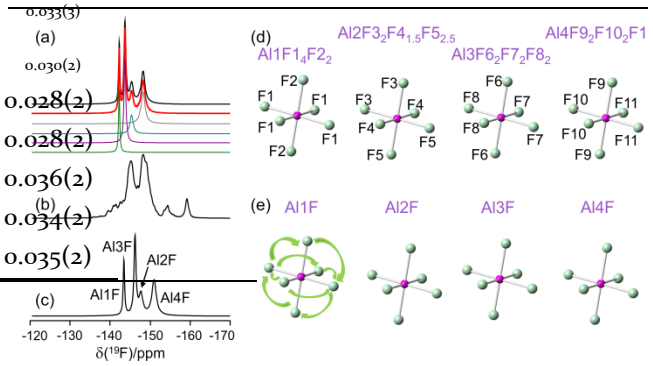

Figure 4. (a) Experimental (black) and simulated (color lines) ^{19}F MAS NMR spectra of α-Rb_3AlF_6 at 20 T. (b) Sum of seventeen ^{19}F spectra reconstructed with a set of the calculated chemical shift parameters (all full width at half-maximum, FWHM=0.5 ppm). (c) ^{19}F spectrum reconstructed (only isotropic resonances) using average fluorine positions for each of the calculated structures. (d) Structural arrangements around aluminum atoms. (e) Schematic representation of the dynamics of F atoms in AlF_6 octahedra.

Table 3. ^{87}Rb isotropic chemical shift (δ_{iso}), mean quadrupolar constants (C_Q), and relative intensities obtained from the simulation of the ^{87}Rb MAS and MQMAS at 9.4 T and 20 T.

Rb line	δ_{iso}, ppm (±0.2 ppm)	C_Q, MHz (±0.1 MHz)	η_Q (±0.1)	Integral intensity, % (±2%)

5	44.7	5.3	0.6	18
4	42.2	6.2	0.65	17
3	18.6	5.3	0.5	30
2	14.1	3.8	0.5	12
1	-22.4	2.7	0.8	23

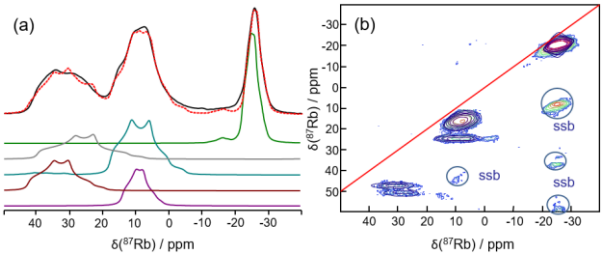

Figure 5. (a) Experimental (black) and simulated (color lines) ^{87}Rb MAS NMR spectra, (b) ^{87}Rb MQ MAS experimental (color lines) NMR spectrum of Rb_3AlF_6 at 20 T and spinning rate of 30 kHz and its simulation (black line) with the parameters presented in Table 3 (ssb stands for spinning side bands).

A description of the potassium environment in γ-K_3AlF_6 was reported by King *et* al.[8] In α-Rb_3AlF_6, half of the Rb1 atoms is 7-coordinated while the other half of atoms shows a 6-coordinated octahedral environment. Rb2 atoms are 7-coordinated. Rb3, Rb4, and Rb5 atoms are each surrounded by 10, 11 or 12 fluorine atoms, due to partial occupancy of F3, F4, and F5 sites. Consequently, six ^{87}Rb resonances with relative intensities of 1 for ½ $Rb1F_6$, 1 for the second ½ $Rb1F_7$, 1 for Rb2, and 2/2/2 for Rb3/Rb4/Rb5 were expected on the ^{87}Rb MAS NMR spectrum. However, only three broad peaks were observed (Figure 5a).

The MQMAS NMR spectrum provides a better resolution. In fact, five resonances, which are overlapped on the 1D NMR spectrum, are now clearly distinguish (Figure 5b). The resonances are in the range -20 to 40 ppm. The only reported ^{87}Rb NMR spectra in literature are that of RbF and a $RbLaF_4$. Rubidium fluoride adopts a cubic structure with RbF_8 coordination (resonance is located at 19.1 ppm).[35] The structure of $RbLaF_4$ contains a RbF_7 edge-tricapped trigonal prism. The rubidium resonance at 51.1 ppm has a quadrupolar broadening with C_Q value of 10.97 MHz and η_Q value of 1.[36] It means that there is no established relationship between the coordination number of the rubidium cation and their chemical shift. In the case of $RbAlF_4$, the rubidium atoms, like in RbF, have eightfold cubic coordination environments. The ^{87}Rb NMR $RbAlF_4$ spectrum shows a single resonance at 1.8 ppm (see Figure S6). In an attempt to better understand and assign the ^{87}Rb NMR spectrum of α-Rb_3AlF_6, we also recorded a ^{87}Rb–^{19}F D-HMQC HETCOR MAS NMR spectrum (see Figure S7). The strong overlap of the ^{87}Rb resonances, however, did not allow any further assignment of the resonances.

First-Principles Calculations.

In order to confirm the structure of α-Rb_3AlF_6 and to gain a better understanding of the discrepancy regarding the ^{19}F NMR spectra, a GIPAW calculation of the NMR parameters was performed. Since CASTEP cannot handle partial occupancies of fluorine F3, F4 and F5, a set of structures (compatible with the experimental site occupancy factors) were at the beginning generated by a combinatorial approach.[37] The whole set of combinations of a supercell, which is in this case 213744. This is too big to be able be processed it in one single step. Figure 6a depicts a chart of the electrostatic energies, which are lined up by rising order of all structures. The minimum calculated Coulomb energy (Ec_{min} = -1188.6 eV) was taken as a base to which the energy values are relative to circa 59 eV (a whole extent of the distribution of the calculated energies). Figure 6b is aiming to the 250 lowest-Ec structures, where we hope, the best correlation with the real system, can be found. The initial 10 lowest-Ec and every 20 up to 200 structures were selected for further optimization. The optimization of the geometry of the last three structures (ranked 160th, 180th, and 200th), was not however reached, even after one week of iterations. It was due to a strong movement of fluorine atoms from the initial positions.

The final outcome is based on 17 structures. All calculated ^{19}F δ_{iso} are shown in Figure 4b, where the comparison to the experimental MAS NMR spectrum can also be seen. The disapproval between the experimental and calculated data is larger than what is generally considered as a normal for inorganic fluorides. This discrepancy may has arisen either from bad position of atoms in the unit cell, or from dynamic effects that had not been taken in to the GIPAW calculations. Because SPD refinements had not given a clear proof for residual electron density, we inquired the dynamic-reorientation hypothesis. This hypothesis is based on the fact that isolated AlF_6 polyhedra in inorganic fluorides can display, even in room temperature, a reorientation (dynamic rotations of the AlF_6 octahedra).[39]

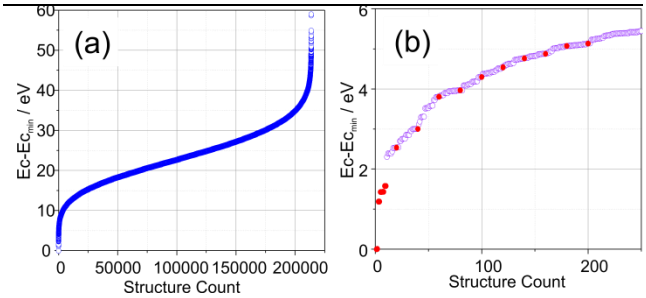

Figure 6. (a) A chart of the electrostatic energies (E_C) of the 213744 distinct structural models lined up by rising order of all structures. (b) Extended view of the 250 structures of lowest E_C. The first 10 lowest-E_C and every 20-200 structures, shown as red circles, were chosen for further calculations.

By analyzing the Al environments, one can notice that the four Al atomic positions have two or three distinct fluorine atoms in their coordination spheres: $Al1F1_4F2_2$, $Al2F3_2F4_{1.5}F5_{2.5}$, $Al3F6_2F7_2F8_2$ and $Al4F9_2F10_2F11_2$. Considering fast hoping of the fluorine on each position around one AlF_6 octahedron, the ^{19}F δ_{iso} is then the barycenter of the

individual δ_{iso}. We suppose that the fluorine atoms change their positions between the crystallographic sites by flipping. Since motion is not introduced in CASTEP, we can simply average the fluorine positions on each of the calculated structures. The multiplicities of the Al1:Al2:Al3:Al4 sites are 1:1:2:2, and expected integral intensities agree well with the experimental values. The overall good agreement between the reconstructed and experimental ^{19}F spectrum enables to perform accurate spectral assignment of the NMR resonances with the crystallographic sites. This last result enables validation of i) the structural model and ii) the fast hoping hypothesis occurring at room temperature. To reconstruct the ^{19}F spectrum, the line widths (FWHM) were used corresponding to the experimental values. Note that the obtained average isotropic magnetic shielding values σ_{iso} for fluorine atoms have very close values (±0.7 ppm), which allows us to assert that increasing the number of structures used for prediction will not significantly change the final result. Seventeen structures are enough to image the real structure.

The fast motion of fluorine atoms is also responsible for the small C_Q value observed for the ^{27}Al resonances, when the calculated values range 1-8.2 MHz. This motion is also responsible for the uniqueness of all 4 Al resonances. Regarding rubidium atoms, the analysis of the DFT calculations could not be done since each Rb atom has in its coordination sphere several fluoride ions coming from different AlF_6 polyhedra, each one having independent dynamics.

These dynamic rotations of the AlF_6 octahedra were observed in δ-K_3AlF_6 phase, and it was supposed that such rotations could be occurring in some of the lower temperature phases as well.[8] Our data confirms this supposition.

β-Rb_3AlF_6

High-Temperature synchrotron powder diffraction data.

In order to track the α-Rb_3AlF_6 to β-Rb_3AlF_6 phase transition, observed by thermal analysis around 350 °C, high-resolution synchrotron powder diffraction diagrams were collected (Figure 7) from room temperature up to 600 °C (using 100 °C steps). The phase transformation between 300 °C and 400 °C was also observed.

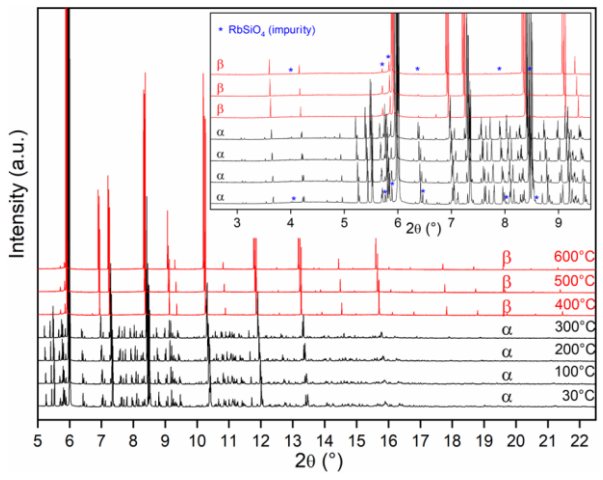

Figure 7. Synchrotron powder diffraction patterns of Rb_3AlF_6 recording as a function of temperature upon heating. The diagrams corresponding to low temperature form (orthorhombic *Fddd* with *a*=37.26491(1) Å, *b*=12.45405(4) Å and *c*=17.68341(6) Å) and high temperature form (cubic *Fm*-$\bar{3}$*m* with *a*=8.9930(2) Å) are indicated by α and β symbols respectively.

The same procedure, as used for the room temperature polymorph, was applied to solve and refine the crystal structure of the high temperature polymorph (data recorded *in-situ* at 600 °C). A cubic unit cell with *a* = 8.9930(2) Å was determined from auto indexing routines, whereas the most symmetric *Fm*-$\bar{3}$*m* space group was found suitable for the high-temperature β-Rb_3AlF_6 polymorph. An isostructural model could be identified, namely δ-K_3AlF_6 (ICSD 262078). The structure refinement was therefore performed using this structural model as starting point using a Rb substitution for K atomic positions and isotropic thermal factors for Rb, Al and F. The refinement converged to low R_B-factor values of (Figure 8) (R_{wp}=7.92 %, R_p=4.70 % and GOF=0.89). The main results of the Rietveld refinement are reported in Table 4.

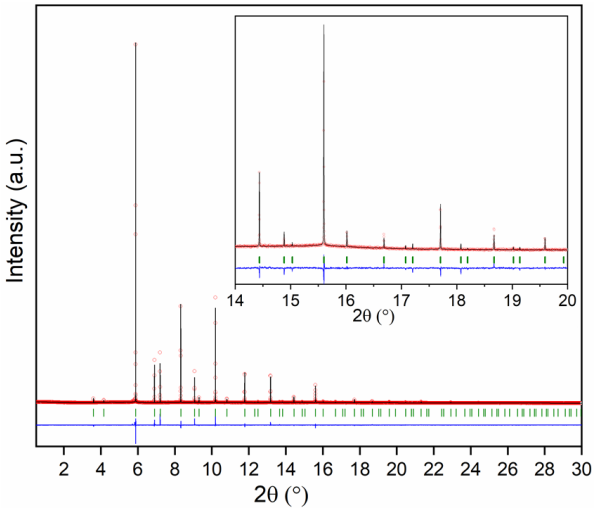

Figure 8. Rietveld refinement of the SPD pattern of β-Rb_3AlF_6 collected at 600 °C. Experimental (red), calculated (black), difference (blue) and Bragg reflections (cubic *Fm*-$\bar{3}$*m* *a*=8.9930(2) Å) (green marks) are represented.

Table 4. Atomic coordinates and Atomic Displacement Parameters of β-Rb_3AlF_6 determined from *in-situ* Rietveld Refinement of synchrotron powder diffraction data collected at 600 °C.

Atom	Wyckoff site	Occupancy	x/a	y/b	z/c	U_{iso} / Å²
Rb1	8c	1	0.25	0.25	0.25	0.0676(3)
Rb2	4b	1	0.5	0.5	0.5	0.0685(4)

Al1	4a	1	0	0	0	0.0531(1)
F1	24e	1	0.2002 (2)	0	0	0.1110(1)

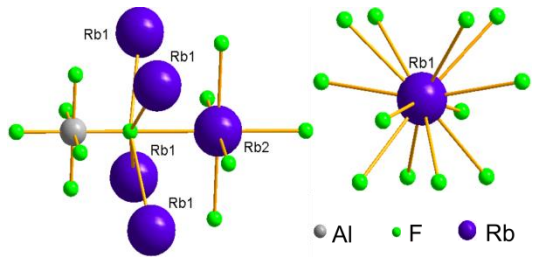

Figure 9. Structural arrangements around aluminum, fluorine, and rubidium atoms.

β-Rb_3AlF_6 has an ideal cubic structure of a double perovskite with space group $Fm\text{-}\bar{3}m$. The AlF_6 octahedra are centered at the origin and the face centers of the cubic cell. Rubidium atoms adopt an RbF_6 and RbF_{12} coordination (Figure 9).

The fluorine atomic displacement parameter (ADP) is very large (U_{iso} = 0.111 Å^2), which might reflect static or dynamic disorder. This large value was previously observed in case of δ-phase of K_3AlF_6.[8] Based on reverse Monte Carlo simulations, the authors[8] explained the large anisotropy of the fluorine ADPs by significant rotations of AlF_6 octahedra. It can be noted that disorder on F atomic positions was also previously reported in the β sodium cryolite.[5]

High-Temperature MAS NMR data.

β-Rb_3AlF_6: As it was shown previously, the room temperature ^{19}F MAS NMR spectrum of Rb_3AlF_6 (α-phase) has shown four isotropic resonances. At the low MAS frequency (5 kHz, required for the HT measurements) and high field (17.6 T), numerous spinning sidebands are presented due to the chemical shift anisotropy (Figure S8). Therefore, the MATPASS pulse sequence was used. As it was expected, the resolution of the room temperature ^{19}F MATPASS NMR spectrum recorded at 5 kHz MAS frequency is much lower than at 30 kHz, but still the four ^{19}F resonances can still be distinguished (Figure 10). For ^{87}Rb, the 30 kHz MAS and 5 kHz QMATPASS NMR spectra are identical. ^{19}F MATPASS and ^{87}Rb QMATPASS NMR spectra were recorded in the temperature range RT < t ≤ 352 °C (Figures 10 and 11). For higher temperature, the transverse relaxation time significantly decreased, so that the intensity of the echo signal after three rotor periods was too small to carry out the side band separation. Therefore, in the range 363 °C < t < 600 °C, the MAS NMR spectra were recorded using a single pulse excitation. A complete reversibility, without hysteresis of the spectral changes, was observed.

It is worth noting that room temperature MAS NMR measurements were performed without temperature regulation. Due to frictional heating, the real temperatures of the sample were 32 °C at 5 kHz MAS and 56 °C at 30 kHz.

The ^{19}F lines were, upon slight heating (90 °C), significantly sharpened, which confirmed the facile motion of the fluoride anions in the structure. A further sharpening of the ^{19}F resonances (and also small shift) is visible while heating up to the phase transition temperature (Figure 10, left). At the phase transition temperature (352 °C), an additional peak at -143.7 ppm appears, which is corresponding to the initial formation of the β-phase. This phase contains a single crystallographic F site. The coexistence of both α- and β-polymorphs can be seen in the 352-363 °C range (Figure 10). The presence of both phases was possible due to a temperature gradient in the body of the sample. One can notice that the ^{19}F resonance of the β-phase has spinning sidebands, indicating limited fluorine motion up to 375 °C (Figure 10, blue spectrum in the right). A fast fluorine motion, above this temperature, can be seen with an absence of spinning sidebands.

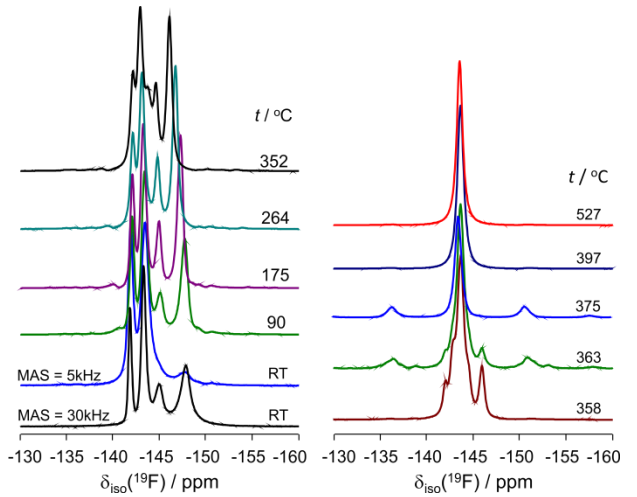

Figure 10. ^{19}F NMR spectra of Rb_3AlF_6 acquired at 17.6 T and MAS 5 kHz as a function of temperature: Isotropic slices of MATPASS for t ≤ 358 °C and one pulse for t > 358 °C.

A dynamic exchange between rubidium units could be clearly identified from the temperature dependent line shape evolution in the ^{87}Rb MAS NMR spectra (Figure 11). Above 175 °C, the 2-5 rubidium resonances broaden and then disappear, indicating the occurrence of dynamic exchange. It should be noted that one line does not change and, therefore, one of the rubidium site does not participate in this exchange. Quantitative analysis of the exchange is hampered by the strong overlap of the 2-5 resonances. Above the phase transition temperature, a new ^{87}Rb resonance appears at 0.7 ppm, corresponding to the β-phase. Up to 363 °C, the coexistence of both phases is confirmed. The phase transition from the room-temperature α-phase to the high temperature β-phase is clearly revealed in the ^{19}F and ^{87}Rb NMR spectra at 352 °C. This temperature range also matches the transition temperature measured by DSC.

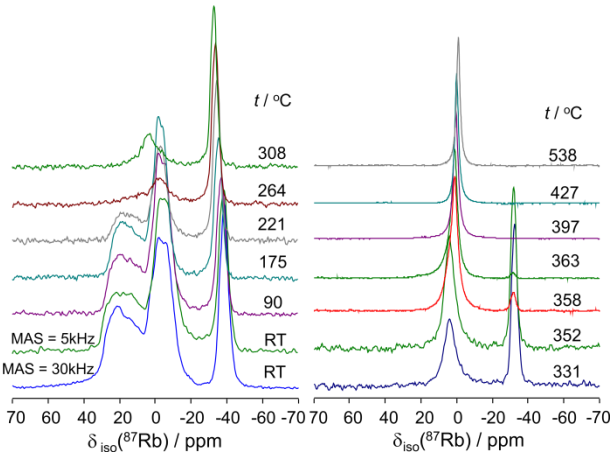

Figure 11. ^{87}Rb NMR spectra of Rb_3AlF_6 at 17.6 T and MAS 5 kHz as a function of temperature: Isotropic slices of QMATPASS for T ≤352 °C and one pulse for T >352 °C.

The ^{19}F and ^{87}Rb spectra recorded at 397 °C exhibit an extremely narrow (FWHM ~750 Hz for ^{87}Rb and ~550 Hz for ^{19}F) singlet resonance without any spinning sidebands. The rubidium and fluorine signals were simulated by one Gaussian line with a chemical shift at 0.7 ppm and -143.7 ppm at T= 397 °C, respectively. From this observation and the fact that there are two rubidium sites in the structure, we conclude that the rubidium sites in β-Rb_3AlF_6 are involved in chemical exchange process. The calculated ^{19}F chemical shift value is -153.5 ppm and it is in reasonably good agreement with our experimental result.

K_3AlF_6: Using the heating of the sample in the MAS NMR rotor by a laser beam, the ^{19}F MAS NMR spectra of all four polymorphs (α→β 132 °C; β→γ 153 °C; γ→δ 310 °C) of K_3AlF_6 could be recorded (Figure 12). The room temperature polymorph α-K_3AlF_6 adopts the elpasolite structure (ICSD 260574).[7] It contains 5 Al sites in slightly distorted octahedral environments, 18 potassium crystallographic sites and 30 crystallographically nonequivalent fluorine sites, and consists of symmetrically equivalent layers of the AlF_6 units. Every layer contains the octahedra rotated by $\pi/4$ around the *c* and *a* or *b* axes (non-cooperative octahedral tilting, NCOT). As previously reported, the ^{19}F MAS NMR spectrum at 60 kHz and 20 T consists of a broad envelope of signals in the -156 to -160 ppm range and four small signals at -162, -164.1, -167.3, and -168.5 ppm.[18] It was not possible to make an assignment of lines to F sites. The α phase is stable up to 132 °C and further transforms into the tetragonal β-phase (ICSD 262076), which is stable up to 153 °C. The structure of β-K_3AlF_6 contains seven F and two Al crystallographic sites with multiplicities of 8:4:8:8:8:8:8 for F and 2:8 for Al atoms. Its ^{19}F MAS NMR spectrum contains an asymmetrically broadened peak with non-Lorenzian lineshape at -160.1 ppm. As in case of α polymorph, the assignment of ^{19}F signals cannot be provided. In the range 153-306 °C, the orthorhombic γ phase (ICSD 262077) exists. The crystalline structure of γ-K_3AlF_6 contains eleven fluorine sites. The ^{19}F MAS NMR spectrum, recorded at 160 °C, contains four signals at -158.2, -159.2, -160.3 and -161.9 ppm with relative intensities of 15/36/17/32, fewer resonances than expected. This again very likely arises from fast dynamics of fluoride ions. The last phase transition occurs above 306 °C. The high temperature cubic δ phase (ICSD 262078) has double-perovskite structure and it is stable up to the melting temperature of 974 °C.[39] δ-K_3AlF_6 exhibits one kind of fluorine atom, one kind of aluminum atom, and two kinds of potassium atoms. Two potassium atoms are in a 1/2 ratio. The ^{19}F MAS NMR spectrum measured at 335 °C exhibits, as expected, a narrow (FWHM ~550 Hz) singlet resonance at 159.4 ppm.

The both high temperature solid-state ^{19}F NMR spectra of γ-K_3AlF_6 and α-Rb_3AlF_6 contain four lines with the integral intensity ratio of 1:2:1:2. Only one resonance was observed in the flour spectra of γ-K_3AlF_6 and β-Rb_3AlF_6. Thus, NMR data obtained for potassium and rubidium cryolites confirms that α-Rb_3AlF_6 is isostructural to γ-K_3AlF_6 and β-Rb_3AlF_6 is isostructural to δ-phase of K_3AlF_6. We suppose the existence of low temperature phases of Rb_3AlF_6 at temperatures below room temperature, which are isostructural to α- and β-K_3AlF_6.

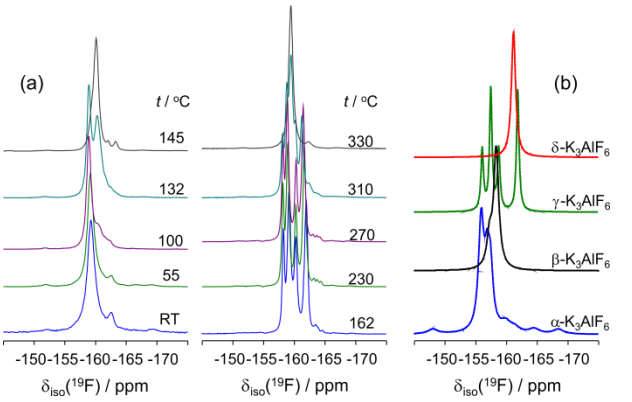

Figure 12. a) Isotropic slices of ^{19}F NMR MATPASS spectra of K_3AlF_6 acquired at 17.6 T and MAS 5 kHz as a function of temperature. b) Reconstructed ^{19}F NMR spectra of polymorphs of K_3AlF_6 (only isotropic resonances).

Figure 12b shows the reconstructed ^{19}F spectrum of polymorphs of K_3AlF_6. The calculation methods are presented in the Supporting Information. Our calculated data show good agreement with ^{19}F NMR results.

The cryolite mineral, Na_3AlF_6, adopts at room temperature (α-form)[4] a monoclinic structure, which consists of an isolated AlF_6 octahedra interconnected by Na atoms. The AlF_6 octahedron is in this structure very regular. Each bond distance and angle does not differ very much from the respective mean value. When we substitute the Na^+ ions by other alkali cations (K^+, Rb^+ in particular), the cryolite structure will changing, as much as the radius of the alkali metal cation. In these systems, the substitution leads to a lattice distortion due to a rotation of the fraction of the AlF_6 octahedral units, which are rotated over a large angle of ~45°. NCOT leads to an increase of the coordination number of the alkali atoms (from 6 up to 12) as it can be seen in our case. Moreover, the substitution also causes the decrease

of the phase transition temperature, so the highly symmetrical α-Rb_3AlF_6 tends to be a stable even at low temperature. The size of the alkali anions is a key factor in the structural relations as well as the physico-chemical behavior of these elpasolite-related fluoride phases.

The following structures exhibiting NCOT have been so far reported: K_3AlF_6,[7,8] Sr_3WO_6,[14] $Rb_2K(Cr\ or\ Ga)F_6$,[15] and $(K\ or\ Rb)_3MoO_3F_3$.[16] These species contain several NMR active isotopes (^{17}O, ^{19}F, ^{27}Al, $^{69/71}Ga$, ^{87}Sr, $^{85/87}Rb$) that typically allow probing their environment by solid-state NMR spectroscopy. To our knowledge, such an experiment has not yet been however reported. Also DFT calculations of NMR parameters of these compounds are missing in open literature. We think that the major reasons, why this information is still not available, relates to the difficulties to correctly interpret the NMR data. The local dynamics taking places in these structures via NCOT effect, is probably the main reason why it is so difficult to interpret the NMR. The DFT calculations can usually help to explain confusing experimental data. However, the atomic positions with partial occupation can also lead to other problems. This study was the first attempt with a demonstration how solid state NMR methods coupled with computations provide the useful insights into the nature of local dynamics that accompanying the structures with the non-cooperative octahedral tilting effect.

CONCLUSIONS

Synchrotron powder diffraction, solid-state NMR spectroscopy, electron diffraction, and first-principles calculations have been used as a coupled approach to perform a complete structural characterization of the two polymorphs of rubidium cryolite Rb_3AlF_6. The structure of α-Rb_3AlF_6 is part of a small family of compounds with non-cooperative octahedral tilting. Variable temperature MAS NMR studies enable the observation of chemical exchange between rubidium sites in α-Rb_3AlF_6. High temperature NMR measurements show that α-Rb_3AlF_6 is isostructural to γ-K_3AlF_6 and β-Rb_3AlF_6 is isostructural to δ-K_3AlF_6. Diffraction-based methods coupled with NMR spectroscopy and DFT calculations was proved as a promising approach to obtain the information about the local dynamics of AlF_6 octahedra with the non-cooperative octahedral tilting.

ACKNOWLEDGMENT

This study was financially supported by CAMPUS FRANCE (PHC STEFANIK project N° 31799NM), the Slovak bilateral project (N° SK-FR-2013-0039), and Slovak Grant Agencies (VEGA-2/0060/18, APVV-15-0738), and ITMS project (with code 313021T081) supported by Research & Innovation Operational Programme funded by the ERDF. For DFT calculations, we thank the "Centre de Calcul Scientifique en region Centre" (Orléans, France). We acknowledge the ICMN (Orléans, France) for access to their Transmission Electron Microscope. Financial support from the IR-RMN-THC Fr3050 CNRS for conducting the research is gratefully acknowledged. We thank also Dr. M.Suchomel and Dr. P.Florian for useful discussions.

ASSOCIATED CONTENT

Supporting Information

Temperature calibration, X-ray powder diffraction patterns of the $RbAlF_4$, thermal analysis diagrams, ^{27}Al MAS NMR, ^{87}Rb MQMAS, ^{87}Rb MAS NMR, 2D D-HMQC MAS NMR, ^{19}F MAS NMR, tables of bond distances (PDF); Crystallographic data (CIF). The Supporting Information is available free of charge on the ACS Publications website.

AUTHOR INFORMATION

Corresponding Authors

* Aydar Rakhmatullin, e-mail: rakhmat@cnrs-orleans.fr, tel.: 0033-238255512 and František Šimko, e-mail: uach-sim@savba.sk, tel.: 00421-2-59410495, fax: 00421-2-59410444

Author Contributions

A.R. and F.S. conceptualized and planned the project. F.S. performed the thermal analysis experiments. E.V. and M.A. performed structural analysis. A.F. performed high temperature XRD experiments. A.R. conducted of the all NMR experiments with assistance from V.S.K., R.S., F.F., and C.B. Z.N., I.B.P. and M.K. performed the synthesis experiments. A.R., K.O., and C.M. carried out the CASTEP calculations. The manuscript was written with contribution from all co-authors.

Notes

The authors declare no competing financial interest.

REFERENCES

(1) Fellner, P.; Haarberg, G. M.; Híveš, J.; Kvande, H.; Sterten, A.; Thonstad, J. *Aluminium Electrolysis: Fundamentals of the Hall-Héroult Process*; Beuth Verlag GmbH, 2001.

(2) L. Holm, J.; Jenssen, B.; Sletten, J.; H. Nielsen, P.; A. Lindberg, A.; Jansen, G.; Lamm, B.; Samuelsson, B. A Note on the Polymorphy and Structure of Li_3AlF_6. *Acta Chemica Scandinavica* **1969**, *23*, 1065–1068.

(3) Garton, G.; Wanklyn, B. M. Polymorphism in Li_3AlF_6. *Journal of Inorganic and Nuclear Chemistry* **1965**, *27*, 2466–2469.

(4) Yang, H.; Ghose, S.; Hatch, D. M. J. P.; Minerals, C. o. Ferroelastic phase transition in cryolite, Na_3AlF_6, a mixed fluoride perovskite: High temperature single crystal X-ray diffraction study and symmetry analysis of the transition mechanism. *Physics and chemistry of Minerals* **1993**, *19*, 528–544.

(5) Smrčok, Ľ.; Kucharík, M.; Tovar, M.; Žižak, I. High temperature powder diffraction and solid state DFT study of β-cryolite (Na_3AlF_6). *Crystal Research and Technology* **2009**, *44*, 834–840.

(6) Bučko, T.; Šimko, F. On the structure of crystalline and molten cryolite: Insights from the ab initio molecular dynamics in NpT ensemble. *The Journal of Chemical Physics* **2016**, *144*, 064502–13.

(7) Abakumov, A. M.; King, G.; Laurinavichute, V. K.; Rozova, M. G.; Woodward, P. M.; Antipov, E. V. The Crystal Structure of α-K_3AlF_6: Elpasolites and Double Perovskites with Broken Corner-Sharing Connectivity of the Octahedral Framework. *Inorganic Chemistry* **2009**, *48*, 9336–9344.

(8) King, G.; Abakumov, A. M.; Woodward, P. M.; Llobet, A.; Tsirlin, A. A.; Batuk, D.; Antipov, E. V. The High-Temperature Polymorphs of K_3AlF_6. *Inorganic Chemistry* **2011**, *50*, 7792–7801.

(9) Holm, J. Phase Transitions and Structure of the High-Temperature Phases of some Compounds of the Cryolite Family. *Acta Chemica Scandinavica* **1965**, *19*, 261–263.

(10) Chen, R.; Zhang, Q. Phase relations in the system AlF_3-RbF. *Thermochimica Acta* **1997**, *297*, 125–129.

(11) Song, E.; Wang, J.; Shi, J.; Deng, T.; Ye, S.; Peng, M.; Wang, J.; Wondraczek, L.; Zhang, Q. Highly Efficient and Thermally Stable $K_3AlF_6:Mn^{4+}$ as a Red Phosphor for Ultra-High-Performance Warm White Light-Emitting Diodes. *ACS Applied Materials & Interfaces* **2017**, *9*, 8805–8812.

(12) Yang, P.; Doty, F. P.; Rodriguez, M. A.; Sanchez, M. R.; Zhou, X.; Shah, K. S. The Synthesis and Structures of Elpasolite Halide Scintillators. *MRS Proceedings* **2009**, *1164*, L1111–1105.

(13) van Eijk, C. W. E. Inorganic Scintillators for Thermal Neutron Detection. *IEEE Transactions on Nuclear Science* **2012**, *59*, 2242–2247.

(14) King, G.; Abakumov, A. M.; Hadermann, J.; Alekseeva, A. M.; Rozova, M. G.; Perkisas, T.; Woodward, P. M.; Van Tendeloo, G.; Antipov, E. V. Crystal Structure and Phase Transitions in Sr_3WO_6. *Inorganic Chemistry* **2010**, *49*, 6058–6065.

(15) Javier Zúñiga, F.; Tressaud, A.; Darriet, J. The low-temperature form of Rb_2KCrF_6 and Rb_2KGaF_6: The first example of an elpasolite-derived structure with pentagonal bipyramid in the B-sublattice. *Journal of Solid State Chemistry* **2006**, *179*, 3607–3614.

(16) Fry, A. M.; Woodward, P. M. Structures of α-$K_3MoO_3F_3$ and α-$Rb_3MoO_3F_3$: Ferroelectricity from Anion Ordering and Noncooperative Octahedral Tilting. *Crystal Growth & Design* **2013**, *13*, 5404–5410.

(17) Zhou, X. W.; Doty, F. P.; Yang, P. In SPIE Optical Engineering + Applications; Doty, F. P., Barber, H. B., Roehrig, H., Schirato, R. C., Eds.; SPIE: San Diego, California, United States, 2010; Vol. 7806, p. 78060E.

(18) Šimko, F.; Rakhmatullin, A.; Florian, P.; Kontrík, M.; Korenko, M.; Netriová, Z.; Danielik, V.; Bessada, C. (Oxo)(Fluoro)–Aluminates in KF–Al_2O_3 System: Thermal Stability and Structural Correlation. *Inorganic Chemistry* **2017**, *56*, 13349–13359.

(19) Šimko, F.; Rakhmatullin, A.; Véron, E.; Allix, M.; Florian, P.; Kontrík, M.; Netriová, Z.; Korenko, M.; Kavečanský, V.; Bessada, C. Oxo- and Oxofluoroaluminates in the RbF–Al_2O_3 System: Synthesis and Structural Characterization. *Inorganic Chemistry* **2018**, *57*, 13702–13712.

(20) Daněk, V.; Čekovský, R. Phase Transitions and Structure of the High-Temperature phases of some Compounds of the Cryolite Family. *Chemical Papers* **1992**, *46*, 161–166.

(21) Trebosc, J.; Hu, B.; Amoureux, J. P.; Gan, Z. Through-space R3-HETCOR experiments between spin-1/2 and half-integer quadrupolar nuclei in solid-state NMR. *Journal of Magnetic Resonance* **2007**, *186*, 220–227.

(22) Gan, Z. $^{13}C/^{14}N$ heteronuclear multiple-quantum correlation with rotary resonance and REDOR dipolar recoupling. *Journal of Magnetic Resonance* **2007**, *184*, 39–43.

(23) Amoureux, J.-P.; Fernandez, C.; Steuernagel, S. ZFiltering in MQMAS NMR. *Journal of Magnetic Resonance, Series A* **1996**, *123*, 116–118.

(24) States, D. J.; Haberkorn, R. A.; Ruben, D. J. A two-dimensional nuclear Overhauser experiment with pure absorption

phase in four quadrants. *Journal of Magnetic Resonance* **1982**, *48*, 286–292.

(25) Hung, I.; Gan, Z. On the magic-angle turning and phase-adjusted spinning sidebands experiments. *Journal of Magnetic Resonance* **2010**, *204*, 150–154.

(26) Hung, I.; Gan, Z. A magic-angle turning NMR experiment for separating spinning sidebands of half-integer quadrupolar nuclei. *Chemical Physics Letters* **2010**, *496*, 162–166.

(27) Ivchenko, N.; Hughes, C. E.; Levitt, M. H. Application of cogwheel phase cycling to sideband manipulation experiments in solid-state NMR. *Journal of Magnetic Resonance* **2003**, *164*, 286–293.

(28) Massiot, D.; Fayon, F.; Capron, M.; King, I.; Le Calvé, S.; Alonso, B.; Durand, J.-O.; Bujoli, B.; Gan, Z.; Hoatson, G. Modelling one- and two-dimensional solid-state NMR spectra. *Magnetic Resonance in Chemistry* **2002**, 40, 70–76.

(29) Lityagina, L. M.; Kabalkina, S. S.; Varfolomeev, M. B.; Losev, V. G. Na_2SiF_6 Polymorphism Under Pressure. *Zhurnal Neorganicheskoi Khimii* **1988**, *33*, 514–517.

(30) Wu, J.; Kim, N.; Stebbins, J. F. Temperature calibration for high-temperature MAS NMR to 913 K: ^{63}Cu MAS NMR of CuBr and CuI, and ^{23}Na MAS NMR of $NaNbO_3$. *Solid State Nuclear Magnetic Resonance* **2011**, *40*, 45–50.

(31) Shakhovoy, R. A.; Rakhmatullin, A.; Deschamps, M.; Sarou-Kanian, V.; Bessada, C. Nuclear magnetic resonance study of sulfate reorientations in $LiNaSO_4$. *Journal of Physics: Condensed Matter* **2016**, *28*, 176003.

(32) Venkatachalam, S.; Schröder, C.; Wegner, S.; van Wüllen, L. The structure of a borosilicate and phosphosilicate glasses and its evolution at temperatures above the glass transition temperature: lessons from in situ MAS NMR. *Physics and Chemistry of Glasses - European Journal of Glass Science and Technology Part B* **2014**, 55, 280–287.

(33) Sadoc, A.; Biswal, M.; Body, M.; Legein, C.; Boucher, F.; Massiot, D.; Fayon, F. NMR parameters in column 13 metal fluoride compounds (AlF_3, GaF_3, InF_3 and TlF_3) from first principle calculations. *Solid State Nuclear Magnetic Resonance* **2014**, *59–60*, 1–7.

(34) Grjotheim, K.; Krohn, C.; Malinovský, M.; Matiašovský, K.; Thonstad, J. *Aluminium Electrolysis-Fundamentals of the Hall-Heroult Process*, Verlag, Dusseldorf, Germany, 1982.

(35) Rees, G. J.; Day, S. P.; Lari, A.; Howes, A. P.; Iuga, D.; Pitak, M. B.; Coles, S. J.; Threlfall, T. L.; Light, M. E.; Smith, M. E.; Quigley, D.; Wallis, J. D.; Hanna, J. V. A multinuclear solid state NMR, density functional theory and X-Ray diffraction study of hydrogen bonding in Group I hydrogen dibenzoates. *CrystEngComm* **2013**, *15*, 8823–8839.

(36) Rollet, A.-L.; Allix, M.; Veron, E.; Deschamps, M.; Montouillout, V.; Suchomel, M. R.; Suard, E.; Barre, M.; Ocaña, M.; Sadoc, A.; Boucher, F.; Bessada, C.; Massiot, D.; Fayon, F. Synthesis and Structure Resolution of $RbLaF_4$. *Inorganic Chemistry* **2012**, *51*, 2272–2282.

(37) Okhotnikov, K.; Charpentier, T.; Cadars, S. Supercell program: a combinatorial structure-generation approach for the local-level modeling of atomic substitutions and partial occupancies in crystals. *Journal of Cheminformatics* **2016**, *8*, 17–25.

(38) Kotecha, M.; Chaudhuri, S.; Grey, C. P.; Frydman, L. Dynamic Effects in MAS and MQMAS NMR Spectra of Half-Integer Quadrupolar Nuclei: Calculations and an Application to the Double Perovskite Cryolite. *Journal of the American Chemical Society* **2005**, *127*, 16701–16712.

(39) Holm, J. L. Phase Transitions and Structure of the High-Temperature phases of some Compounds of the Cryolite Family. *Acta Chemica Scandinavica* **1965**, *19*, 261–262.

(40) Boultif, A.; Louer, D. Indexing of powder diffraction patterns for low-symmetry lattices by the successive dichotomy method. *Journal of Applied Crystallography* **1991**, *24*, 987–993.

(41) Werner, P.-E. Trial-and-error computer methods for the indexing of unknown powder patterns. *Zeitschrift für Kristallographie* **1964**, *120*, 375–387.

Table of Contents Synopsis and Graphic

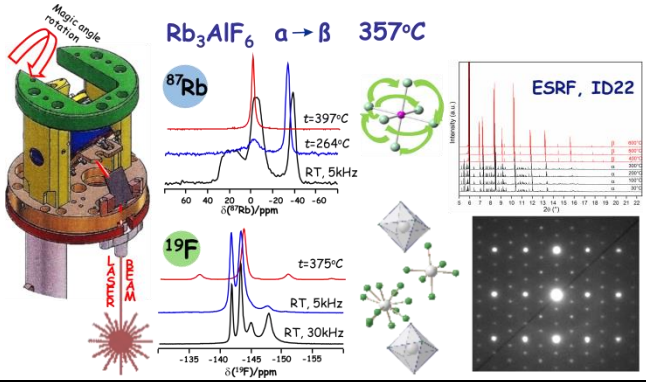

Synopsis:

Insight into the detailed structure of two polymorphs of the rubidium cryolite Rb_3AlF_6 with non-cooperative octahedral tilting was obtained by using a combination of synchrotron powder diffraction, multinuclear high temperature solid-state NMR spectroscopy, electron diffraction, and first-principles calculations.

Dynamic processes such as chemical exchange of rubidium sites and rotations of AlF_6 octahedra are observed and discussed.